


Article

Wavefront Reconstruction of Shack-Hartmann with Under-Sampling of Sub-Apertures

Jian Huang¹, Lianqun Yao², Shuyun Wu³  and Gongchang Wang^{4,*}

- ¹ Chongqing Key Laboratory of Manufacturing Equipment Mechanism Design and Control, School of Mechanical Engineering, Chongqing Technology and Business University, Chongqing 400067, China
- ² Institute of Optics and Electronics, Chinese Academy of Sciences, Chengdu 610209, China
- ³ Southwest Institute of Technical Physics, Chengdu 610014, China
- ⁴ Xi'an Satellite Control Center, Xi'an 710043, China
- * Correspondence: wh-99@126.com

Abstract: Shack-Hartmann wavefront sensor plays a key role in adaptive optics (AO) systems, which detect the aberrant wavefront by an array of micro-lenslets across the aperture pupil. However, some sub-apertures would be a lack of light induced by the imperfectness of micro-lenslets or pupil shift away from the optical path. Thus, the wavefront detection would be under-sampled and the performance of wavefront reconstruction would be severely degraded. It is therefore important to evaluate the influence of under-sampling on the wavefront reconstruction. In this paper, an AO system was established by the OOMAO simulation platform. For dynamical turbulence aberrations or statistic defocus aberrations, three cases including a single sub-aperture, a row of sub-apertures, and a quadrant sub-apertures lack of light were simulated. Compared with the uncorrected aberrant wavefront, our results showed that the RMS of the residual wavefront for a typical atmospheric condition (Fried parameter (r_0) ranges from 5 cm to 15 cm) can be reduced by a factor of 5~8, 4~6, and 2~3 with these three cases of under-sampling, respectively.

Keywords: shack-hartmann wavefront sensor; under-sampling; wavefront reconstruction; adaptive optics; weak light



Citation: Huang, J.; Yao, L.; Wu, S.; Wang, G. Wavefront Reconstruction of Shack-Hartmann with Under-Sampling of Sub-Apertures. *Photonics* **2023**, *10*, 65. <https://doi.org/10.3390/photonics10010065>

Received: 10 December 2022
Revised: 3 January 2023
Accepted: 4 January 2023
Published: 6 January 2023



Copyright: © 2023 by the authors. Licensee MDPI, Basel, Switzerland. This article is an open access article distributed under the terms and conditions of the Creative Commons Attribution (CC BY) license (<https://creativecommons.org/licenses/by/4.0/>).

1. Introduction

Over the last two decades, exploring the origin and the future of the universe has become a high scientific priority in astronomical and cosmology areas. In 2020, the institute of high energy physics provided a new way of using spectroastrometry and GRAVITY at the Very Large Telescope (VLT) Interferometer of measuring the Hubble constant (H_0) with high precision ($\leq 3\%$) to test the H_0 tension [1]. The astronomical or cosmology case drives the requirements of the observation by a large aperture ground-based telescope. However, the image quality obtained by the ground-based telescope was degraded by wavefront distortion which originated from the atmospheric turbulence over the earth. The wavefront distortion causes the resolving power of a telescope with several tens of meters in diameter to be only equivalent to that of a telescope with 10~20 cm in diameter [2,3].

In 1953, Adaptive Optics (AO) system was first proposed by Babcock [4]. In the system, a wavefront sensor (WFS) was used to measure the wavefront distortion induced by atmospheric turbulence. Then a wavefront controller calculated an appropriate correction, which was applied to a deformable mirror (DM) in real-time. Later, the aberrant wavefront was reverted to the plane wavefront, and a diffraction-limited image can be obtained. The first step of AO is wavefront sensing, which provides signals to the correctors and affected the performance of the AO system, playing a vital role in the AO system [5]. Currently, Shack-Hartmann (S-H) WFS has become the most popular and widely used WFS in AO systems for astronomical observation [6–8]. It has been used in existing and new-generation telescopes, such as the AO system for the twin Keck telescopes [9], the multiconjugate

adaptive optics (MCAO) for the VLT UT3 and Gemini south [10–13], the MCAO system for the E-ELT (European Extremely Large Telescope) [13].

To sense the wavefront by S-H WFS, the aberrant wavefront was sampled by an array of micro-lenslets across the aperture, producing a pattern of spots in the detector. The aberrant wavefront can be reconstructed by measuring the magnitude and direction of the centroid of each spot, which shifts from its ideal position [3]. The sampling points, namely the number and position of sub-apertures in the micro-lenslets, determine the radial degree and azimuthal frequency of the Zernike polynomials. For example, the tip and tilt can be detected by a single sub-aperture, and the defocus or astigmatism can be detected by 2×2 micro-lenslets [14]. In the condition of the signal-to-noise ratio (SNR) of each sub-aperture larger than 10, as the finite sampling points will influence the performance, the sampling points and sampling frequency are key parameters that influence the performance of the AO system [15].

In 1981, J. Herrmann first discussed that finite sampling caused an interaction between different modes. The concept of an aberration cross-coupling matrix was introduced to describe the cross-coupling of aberrations [15]. In the next two decades, several tests for S-H have been frequently used with different sampling points, such as three, four, or even more [16]. In 2004, A. Zhang et al. analyzed the sampling error under different sampling frequencies (by changing the size of the sub-aperture) of WFS [17]. In 2008, Christoph Baranec and Richard Dekany analyzed the wavefront reconstruction error as a function of pupil sampling of S-H WFS, and optimized the spatial sampling under different values of r_0 [18]. In 2014, Geovanni Hernández-Gómez analyzed the detail of the algorithms that the aberrations reconstructed with three, four, or five sampling points in a circular of an S-H WFS [16]. C. Correia et al. analyzed the aliasing reconstruction errors induced by the spatial sampling frequency, and a theoretical anti-aliasing Wiener filter for wavefront reconstruction in the Fourier domain was presented to overcome this problem [19–21]. In 2017, M. Vieggers proposed a spline-based aberration reconstruction method through moment measurements, which can provide the same accuracy for S-H arrays with reduced spatial sampling sub-apertures [22]. In 2018, to avoid LGS truncation and for a given number of pixels, M. Patti et al. increased the FoV of the sub-aperture by under-sampling, and analyzed the residual aberrations introduced by the effect of under-sampling [23]. In 2020, We Ping et al. compared the wavefront reconstruction error of the slope zeroing and sub-aperture removal recovery methods for the wavefront under-sampled by S-H WFS [24].

Most of the previous works focused on the influence of spatial sampling points on the reconstructed wavefront while assuming that all the sub-apertures were filled with light, or that the SNR of each sub-aperture was larger than 10. However, in practical observations, the sodium laser guide star (LGS) and the natural guide star are not bright enough, or sometimes the detector is not sensitive enough. In this case, the SNR of partial sub-apertures appears to be too low due to the lack of light. On the other hand, the SNR can be decreased by significant noise, such as the scattering light leads to the focal spots disappearing, which can be seen in wavefront measurement for high-resolution imaging for human eye retinal [25,26], or steady focusing of a coherent laser beam passed through the scattering medium using AO system [27,28]. Thus, the confusion between Zernike modes will be severer, and thus the performance of the post-AO system will be significantly degraded.

In this paper, the analysis was based on the 1.2 m- diameter telescope at Yunnan observatory, China [29]. The wavefront under-sampling was caused by partial sub-aperture of S-H WFS, which was a lack of light for a single sub-aperture, a row of sub-apertures, and quadrant sub-apertures in these three cases. We studied identifying the influences of under-sampling on the dynamical turbulence aberrations or statistic defocus aberrations wavefront reconstruction. And hope this work will be of guiding significance to the installation and adjusting of the telescope.

2. Methodology Overview

2.1. Principles of Wavefront Reconstruction

Methods for wavefront reconstruction are classified as a zonal method, modal approach [30], and controlling gradients directly method [31]. Due to the simplification and promising results, controlling gradients directly has become one of the most popular methods for wavefront reconstruction. In this manuscript, our analysis was mainly based on the controlling gradients directly method.

The controlling gradients directly method reconstructed the aberrant wavefront by the wavefront gradients G_x and G_y in each sub-aperture of S-H WFS. If the output of S-H approaches zero, the reconstructive wavefront will be equal to the reference plane wavefront. In this condition, the phase error can be minimized.

The gradients for each sub-aperture in x and y directions can be expressed as:

$$\begin{cases} G_{xi} = \frac{2\pi}{\lambda f} \frac{\sum X_m I_m}{\sum I_m} \\ G_{yi} = \frac{2\pi}{\lambda f} \frac{\sum Y_m I_m}{\sum I_m} \end{cases} \quad (1)$$

where G_{xi} and G_{yi} are the gradients in the x and y directions for the i -th sub-aperture, respectively. X_m and Y_m are the positions of the m -th pixel in the i -th sub-aperture. I_m is the light intensity of the m -th pixel, λ is the wavelength of the LGS, and f is the focal length of the micro-lenslet.

The relationship between the measured gradients and the control voltages applied to the deformable mirror can be expressed as:

$$\begin{aligned} G_{xi} &= \sum_{j=1}^N V_j \frac{\iint \frac{\partial R_j(x,y)}{\partial x} dx dy}{S_i} \\ &= \sum_{j=1}^N V_j R_{xj}(i), \quad i = 1, 2, 3, \dots, M \end{aligned} \quad (2)$$

$$\begin{aligned} G_{yi} &= \sum_{j=1}^N V_j \frac{\iint \frac{\partial R_j(x,y)}{\partial y} dx dy}{S_i} \\ &= \sum_{j=1}^N V_j R_{yj}(i), \quad i = 1, 2, 3, \dots, M \end{aligned} \quad (3)$$

where V_j is the control voltage applied at the j -th actuator of the deformable mirror, N is the total number of the actors, S_i is the normalized area of i -th sub-aperture, $R_j(x,y)$ is the influence function of the j -th actuator, M is the total number of sub-aperture of the S-H WFS, $R_{xi}(i)$ and $R_{yj}(i)$ are the slop influence function of the i -th sub-aperture in x and y directions, respectively. The equation above can also be rewritten as a matrix form

$$\mathbf{G}_c = \mathbf{R}_{xy} \mathbf{V} \quad (4)$$

where \mathbf{G}_c is the matrix of gradients measured by Shack-Hartmann WFS. \mathbf{R}_{xy} is the transfer matrix, which represents the slop response of deformable mirror associated with Shack-Hartmann WFS, and can be obtained by both experimental measurement or theoretical calculation. \mathbf{V} is the matrix of the voltage applied at the actuators of the deformable mirror.

If \mathbf{G} is the measured gradient of the distorted wavefront, according to the least square $\|\mathbf{G} - \mathbf{G}_c\| = \min$ and minimum norm $\|\mathbf{V}\| = \min$, the voltage can be expressed as

$$\mathbf{V} = \mathbf{R}_{xy}^+ \mathbf{G} \quad (5)$$

The reconstructed wavefront can be indicated as:

$$\phi(x, y) = \sum_{j=1}^N V_j R_j(x, y) \quad (6)$$

2.2. Description of Under-Sampling

Three typical cases for the turbulence under-sampling of S-H WFS were shown in Figure 1. Figure 1a shows the under-sampling caused by one sub-apertures lack of light, which was induced by obstructing or damage of the sub-microlens. Figure 1b shows the under-sampling caused by the sub-apertures in the bottom row's lack of light by pupil shifting, which was induced by the primary or other mirrors when they were installed or adjusted. Figure 1c shows the under-sampling caused by a quadrant sub-aperture lack of light induced by the low sensitivity of the detector.

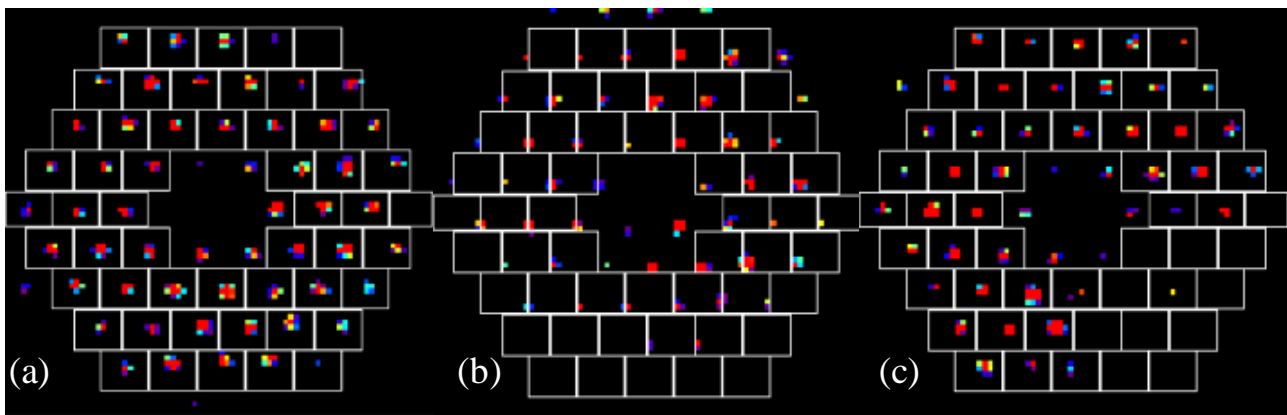


Figure 1. Three typical situations for the wavefront are under-sampled with the sub-aperture of S-H WFS. (a) a single sub-aperture lack of light, (b) a row of sub-apertures at the bottom lack of light, (c) a quadrant sub-aperture lack of light.

3. Numerical Simulation

To analyze the reconstruction performance of an AO system with wavefront sensing under-sampling, a model for sodium LGS AO system was established based on the OOMAO platform, which is a MATLAB toolbox dedicated to AO simulation, it is based on a small set of classes representing the source, atmosphere, telescope, wavefront sensor, Deformable Mirror (DM) and an imager of an AO system, now it has been used for E-ELT and GMT simulation [32]. Additionally, a simulation for the turbulence under-sampled by multi sub-apertures lack of light was conducted.

The atmospheric turbulence was simulated by a random phase screen, which was generated by the power spectral density method. The process of the wavefront propagated in turbulence was based on geometric optics, the distorted phase of the wavefront incident on the pupil was obtained by linear superposition of each phase screen. The sub-apertures lack of light was realized by setting the brightness of the spot on the detector to zero.

3.1. Set Up of the Simulation

The simulation was based on the telescope at Yunnan observatory, the main parameters for the telescope and the S-H WFS were listed in Table 1.

The atmospheric turbulence was described by phase screen with a modal basis. A 5-layer atmosphere with a 10 cm Fried parameter (middle value of the atmospheric coherence length) was created as an example. The standard values of each layer were listed in Table 2. A frame of the phase screen at each altitude was shown in Figure 2.

Table 1. Parameters of the telescope and the AO system.

	Parameters	Standard Value	Description
telescope	D	1.06 m	Diameter of the pupil
	ϵ	0.142	Central obscuration
	r_0	5–15 cm (@550 nm)	Fried parameter
	λ_{obs}	790 nm	Imaging wavelength
S-H WFS	λ	589 nm	Wavelength of the LGS
	-	9×9	Number of sub-aperture
	-	80×80	Pixel number of the camera
Wavefront corrector	-	64	Number of actors
	-	Fried	Configuration of the actors

Table 2. Simulation parameters and their standard nominal values for r_0 of 10 cm.

Layers	Layer 1	Layer 2	Layer 3	Layer 4	Layer 5
Altitude (m)	25	275	425	1250	4000
Wind speed (m/s)	9.4	9.6	9.8	2.78	8.3
Wind direction ($^\circ$)	0.7	8.3	12.5	32.5	72.1
Fractional	0.204	0.112	0.225	0.290	0.169

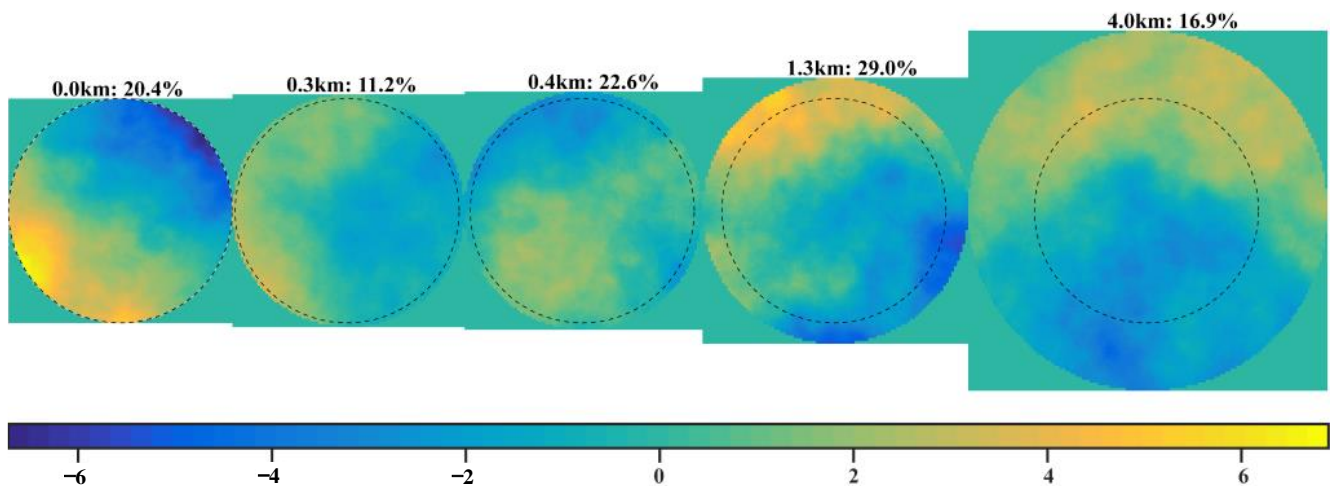


Figure 2. Five phase screens of different layers for the atmosphere with r_0 of 10 cm. The dashed circle line illustrates the diameter of the pupil.

3.2. Simulation of the Turbulence Reconstruction with Under-Sampling of the S-H WFS

In this paper, we have simulated the under-sampling of the wavefront at 3 conditions encountered in our observations: a single sub-aperture numbered 29 was lack of light, as shown in Figure 4a, a row of sub-apertures numbered 43, 44, 48, 49, 50, 51, and 52 had a lack of light, as shown in Figure 4b, a quadrant of sub-apertures numbered 33, 34, 35, 39, 40, 41, 42, 46, 47, 48, 49, 51, 52 had a lack of light, as shown in Figure 4c. As the wavefront reconstruction was based on the detection of the centroid of each spot per sub-aperture, and the brightness of the sodium LGS was higher than the noise, the detector noise can be neglected.

The S-H WFS was modeled with 52 valid sub-apertures, and a minimum ratio of light intensity between a partially and fully illuminated lenslet was set to 0.7. The arrangement of the sub-apertures was shown in Figure 3.

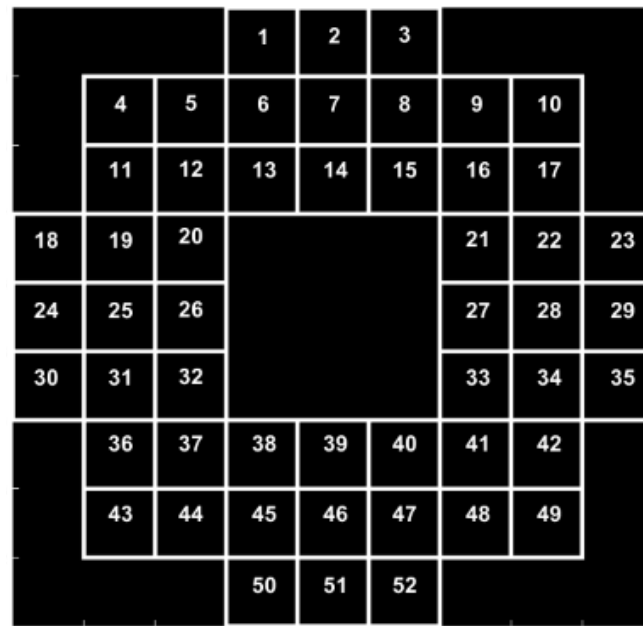


Figure 3. The arrangement and numbers of the sub-apertures of the S-H WFS.

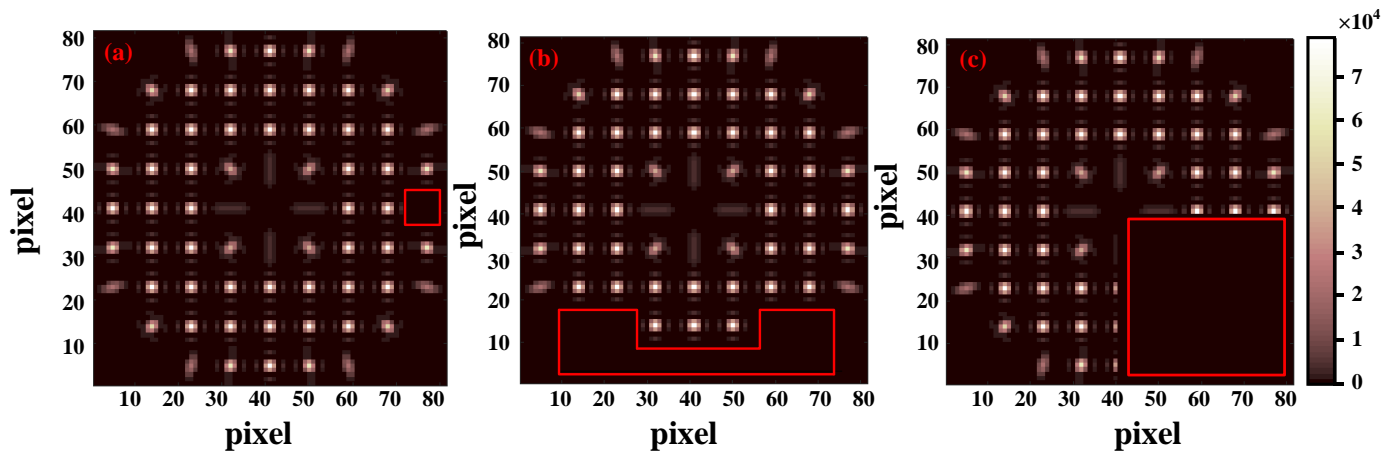


Figure 4. Three cases of under-sampling with sub-apertures lack of light. (a) a single sub-aperture numbered 29 lack of light, (b) a row of sub-apertures numbered 43, 44, 50, 51, 52, 48, 49 at the bottom lack of light, (c) a quadrant sub-aperture numbered 33-35, 40-49, 52 lack of light.

For r_0 is 10 cm, the distorted original wavefront, reconstructed wavefront, and the corresponding residual wavefront were shown in Figure 5. The RMS of the aberrant wavefront is 1.0758λ . The RMS of the residual wavefront with a sampling of all the sub-apertures, under-sampling of one sub-aperture, under-sampling of a row of sub-apertures, and under-sampling of a quadrant sub-apertures are 0.1645λ , 0.1679λ , 0.2390λ and 0.3629λ , respectively. Thus, for a single sub-aperture under-sampling, the negative influence can be negligible. However, with the increasing number of sub-aperture under-sampling, the wavefront reconstruction error rapidly increased.

The corrected image for these 3 cases as shown in Figure 5 at the I band was obtained, as shown in Figure 6. The distorted image without correction was blurred with an SR of 0.2. The SR for the corrected images with no sub-aperture lack of light is 0.73, which is approximating the diffraction limit. The SR for the corrected image with one sub-aperture and a row of sub-aperture under-sampling is 0.72 and 0.62 respectively. However, the corrected image with a quadrant of sub-apertures under-sampling was degraded more obviously than the former two cases, the SR is nearly 0.4, but it is two times higher than the images without corrected.

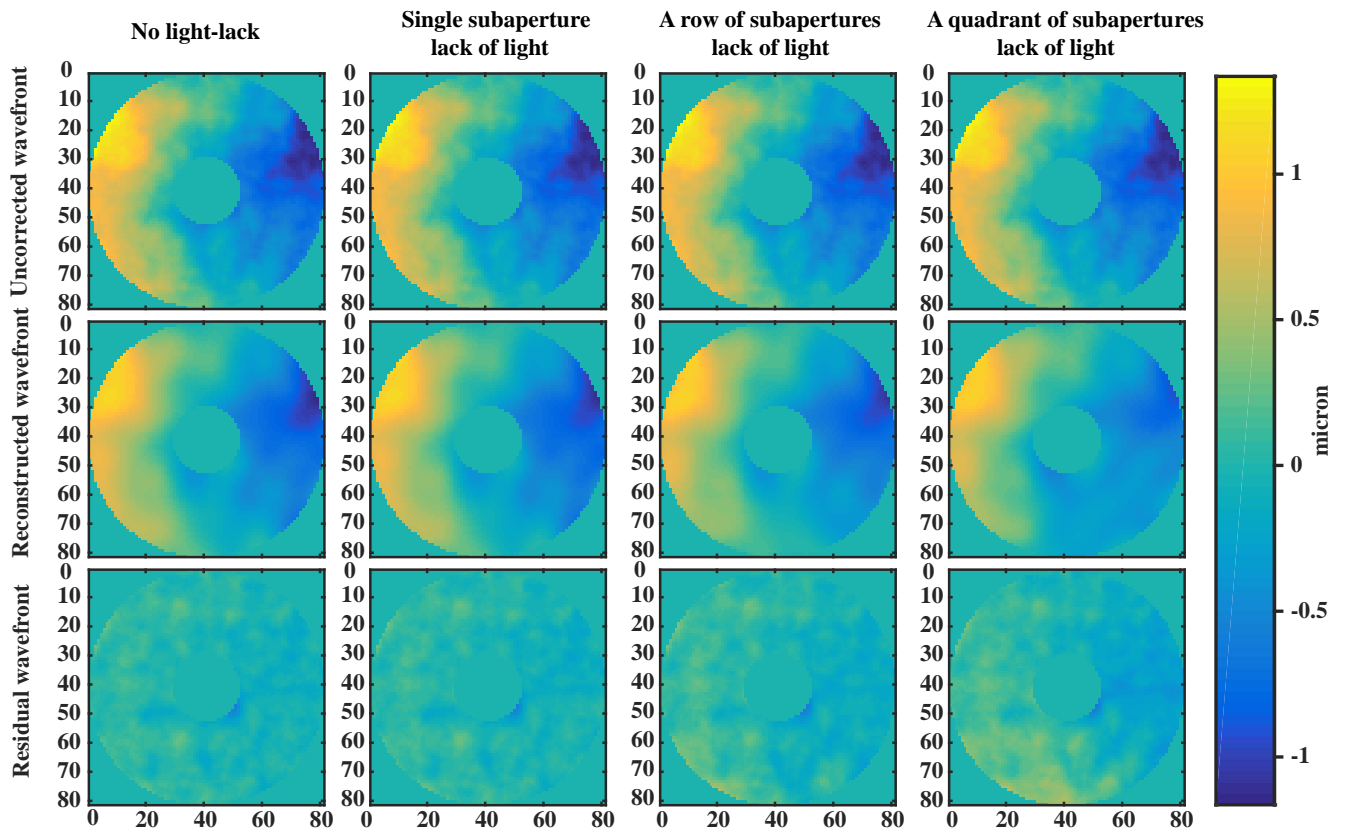


Figure 5. For r_0 is 10 cm, the aberrant wavefront, reconstructed wavefront, and the residual wavefront. The residual error increases rapidly with the increasing number of sub-apertures.

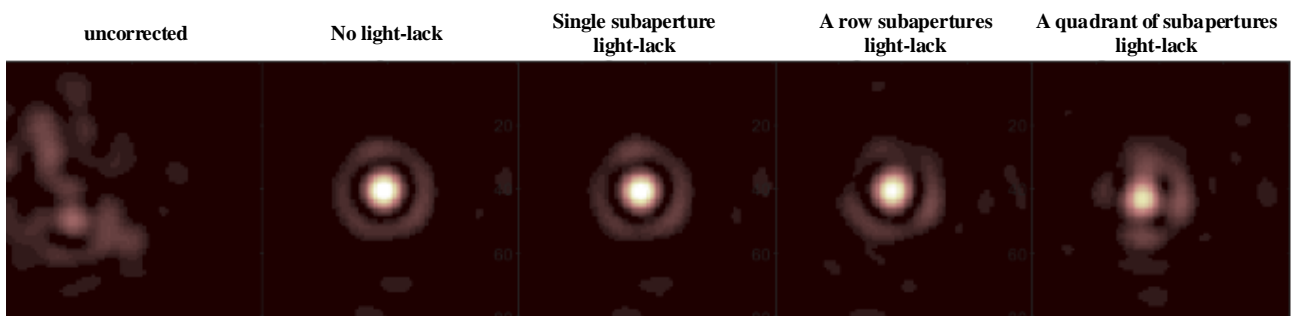


Figure 6. Effected images of a point target in an I-wave band with different light-lack situations.

At the same time, the evolution of the reconstructed wavefront in 200 frames at different values of r_0 was simulated, as shown in Figure 7. The fluctuation of the RMS at different frames was caused by the randomness of the turbulence, with the increasing of r_0 , the smaller the fluctuation was. On the whole, the RMS of the residual wavefront after correcting was increased with the numbers of the under-sampling sub-apertures but decreased with the increase of r_0 . However, the reconstructed wavefront under-sampled with a single sub-aperture lack of light was nearly the same as that of the completed corrected. For the weak turbulence (r_0 is 15 cm), the difference for the three cases with light-lack is smaller, which means the influence of under-sampling is weaker.

In Figure 8, considering only the turbulence aberrations, the RMS of the residual wavefront varies with r_0 was shown. From the curves, we can see that the performance of the AO system was improved with the increase of r_0 . At the condition that the aberrant wavefront is under-sampled by one single sub-aperture at the edge with a lack of light, the performance is equivalent to that of the sub-apertures that were all full of light. The reason is that the slop measurement error will be increased, as the sampling light may not be fully

collected by the sub-aperture at the edge. Additionally, compared with the uncorrected wavefront, the RMS can be reduced by a factor of 5~8, 4~6, and 2~3 for a single sub-aperture, a row of sub-apertures and a quadrant sub-apertures under-sampling, respectively.

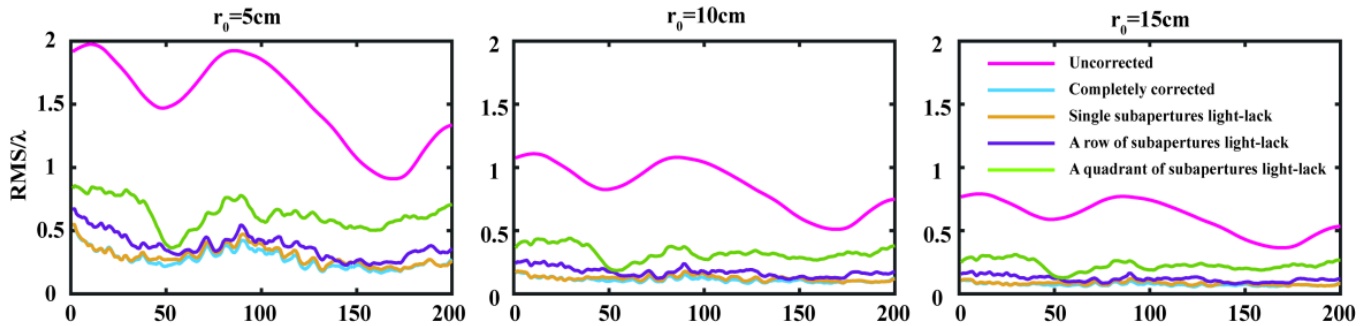


Figure 7. Correction results of 200 frames of different situations of under-samplings, for r_0 , are 5 cm, 10 cm, and 15 cm, respectively. The pinkish-red line represents the uncorrected aberrant wavefront distorted by turbulence. The blue line represents the results that turbulence was corrected with all the sub-apertures illuminated. The yellow line represents a single sub-aperture lack of light. The purple line represents a row of sub-apertures lack of light. The green line represents a quadrant of sub-apertures lack of light.

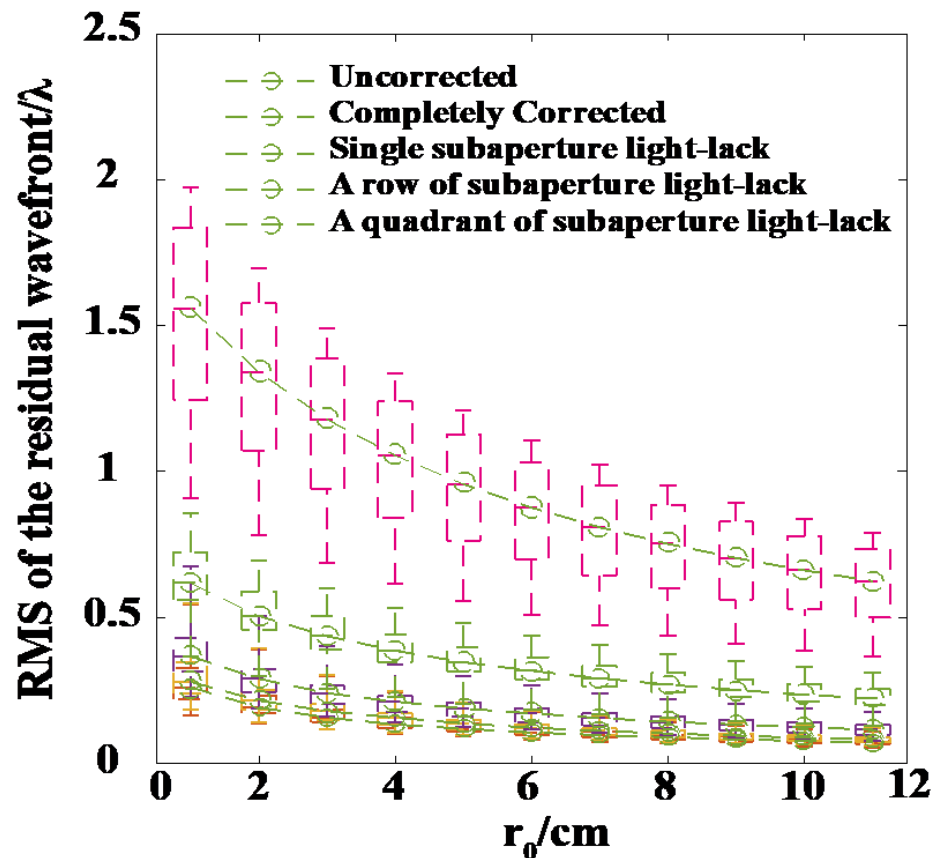


Figure 8. For the case of turbulence aberration, RMS of the residual wavefront varies with different values of r_0 under the conditions of uncorrected, completely corrected, single sub-aperture lack of light, a row of sub-apertures lack of light, and a quadrant of sub-apertures lack of light. Compared with the uncorrected result, the RMS can be reduced by a factor of 5~8, 4~6, and 2~3 at the condition of a single sub-aperture lack of light, a row of sub-apertures lack of light, and a quadrant of sub-apertures lack of light.

4. Discussion

4.1. Influence of the Under-Sampling on the Defocus Statistical Aberration

The defocus is the most common statistical aberration of the telescope during our observation, which can be expressed as:

$$\varphi = \sqrt{3}(2\rho^2 - 1) \tag{7}$$

where $\rho \in [0, D]$, the defocus aberration, was shown in Figure 9. We have discussed the defocus aberration under-sampled at these three conditions, the results were shown in Figure 10. We can see that the reconstructed wavefront under-sampled was influenced by the position of the sub-apertures lack of light. Especially, since the defocus was under-sampled by a single sub-aperture lack of light, the part of the aberration at the position of the under-sampled sub-aperture can not be corrected accurately. Moreover, the edge was corrugated symmetrically. For the wavefront under-sampled with a quadrant of sub-apertures lack of light, the corrugated was mitigated with the increasing numbers of sub-apertures.

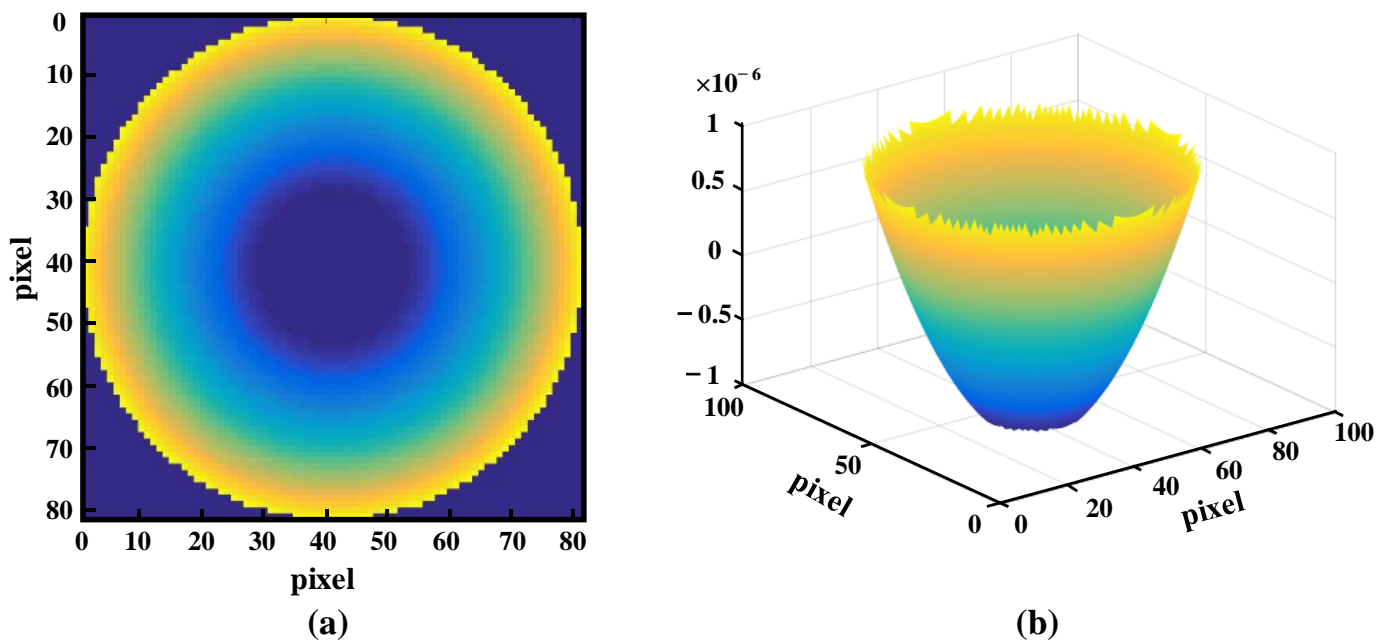


Figure 9. The statistical defocus aberration at the pupil of the 1.2 m telescope (a,b).

4.2. Influence of Under-Sampling on the Mixed Aberrations

In reality, the aberrations corrected by the AO system were mixed with statistical defocus aberration and dynamical aberrations induced by turbulence. In this part, for r_0 is 10 cm, the mixed aberrations were under-sampled and corrected in these three cases. One frame of the results was shown in Figure 11. From the figures, we can see that a single sub-aperture under-sampling has less effect on the residual error. With the increasing number of under-sampled sub-apertures, the residual error had increased. But compared with the statistical defocus aberration, the number and position of the sub-apertures lack of light have less influence, the reason is that compared with the high order Zernike polynomials of the dynamical aberrations, the statistical defocus aberration is varied monotonically from the center.

The evolution of the corrected wavefront for the mixed aberrations in 200 frames had also been simulated, the r_0 was valued at 5 cm, 10 cm, and 15 cm respectively, and the RMS of the corrected wavefront was shown in Figure 12. First and foremost, the reconstructed wavefront with a single sub-aperture under-sampled was nearly the same as

the reconstructed wavefront which was completely sampled. Compared with the reconstructed results of single sub-aperture under-sampling for statistical defocus aberration, the wavefront under-sampling with single sub-aperture has a greater influence on statistical defocus than dynamic turbulence aberrations. Additionally, with the increase of r_0 , the residual error is decreased in these three cases. However, the fluctuation of the curves was more severe compared with the result in Figure 7, the reason was that the under-sampling has a greater influence on regularity aberration, like the defocus aberrations. Lastly, the gain for the RMS of the residual wavefront of mixed aberration is larger than the case of only dynamical aberrations, like for r_0 was 15 cm, the difference of the RMS between the case of uncorrected and the case of a quadrant of sub-apertures light-lack is nearly 0.8, while for the only dynamical aberrations, the difference is nearly 0.4. That means in the observation of reality, the wavefront of the science target was distorted with turbulence and other statistical aberrations in the post-optical path, and the aberrant wavefront was under-sampled, but the image quality can be improved obviously.

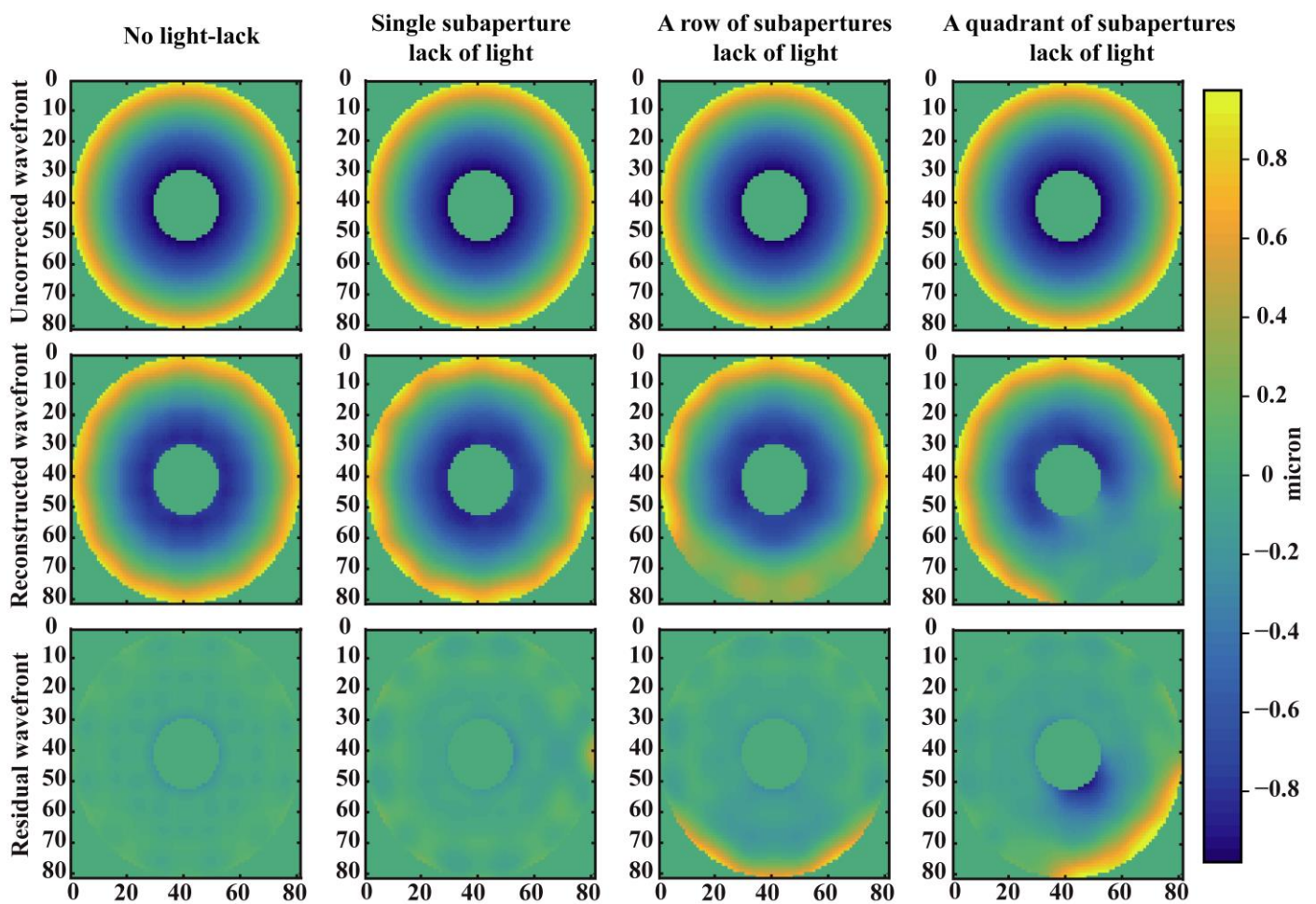


Figure 10. The influence of under-sampling on the statistical defocus in these three cases. The first row is the statistical aberration of defocus, the second row is the reconstructed wavefront under these three cases and the last row is the residual wavefront after correcting the initial defocus.

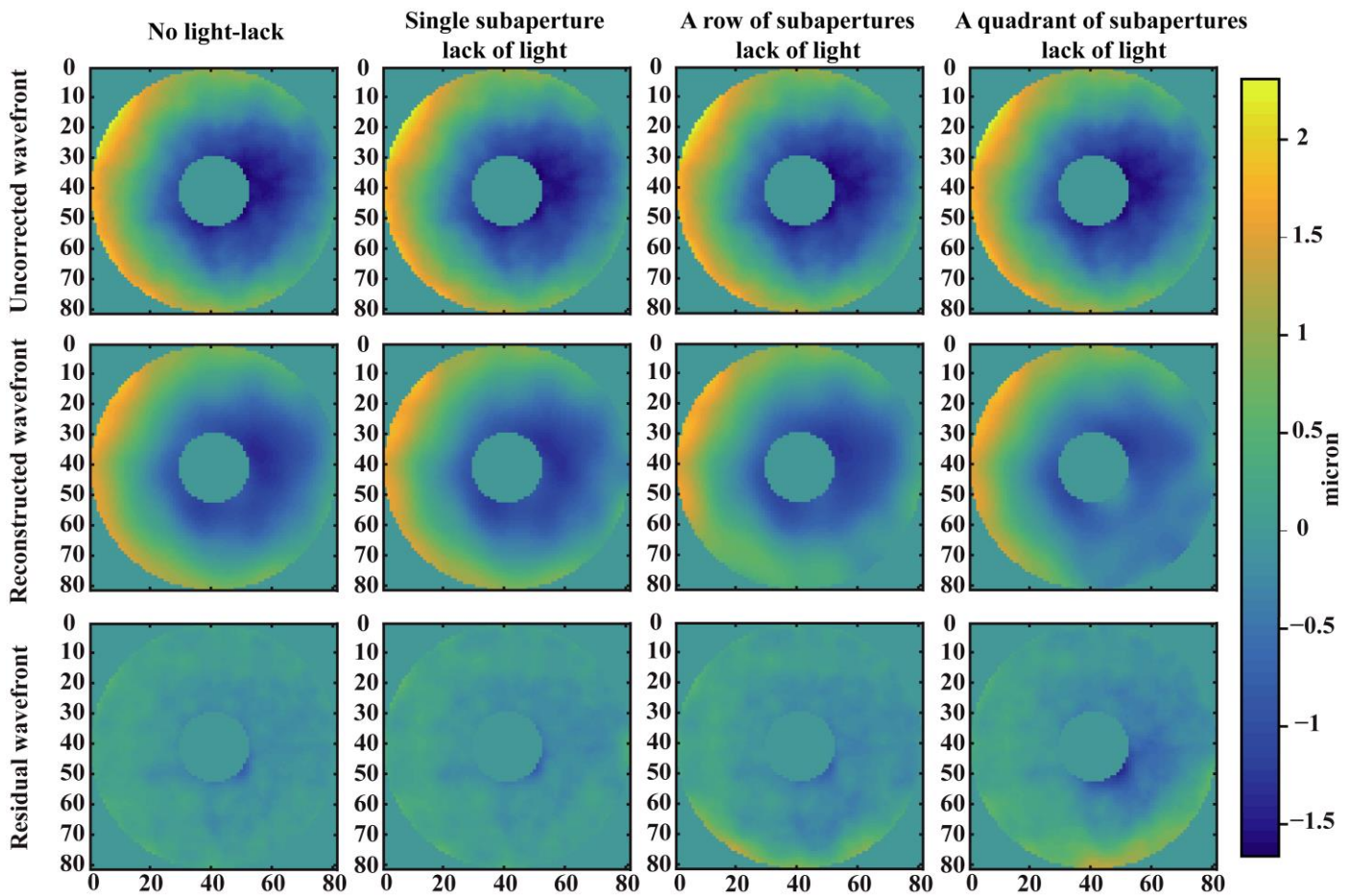


Figure 11. The influence of under-sampling on the mixed aberrations in these three cases. The first row is the initial aberrant wavefront, the second row is the reconstructed wavefront under these three cases and the last row is the residual wavefront after correcting the initially mixed aberrations.

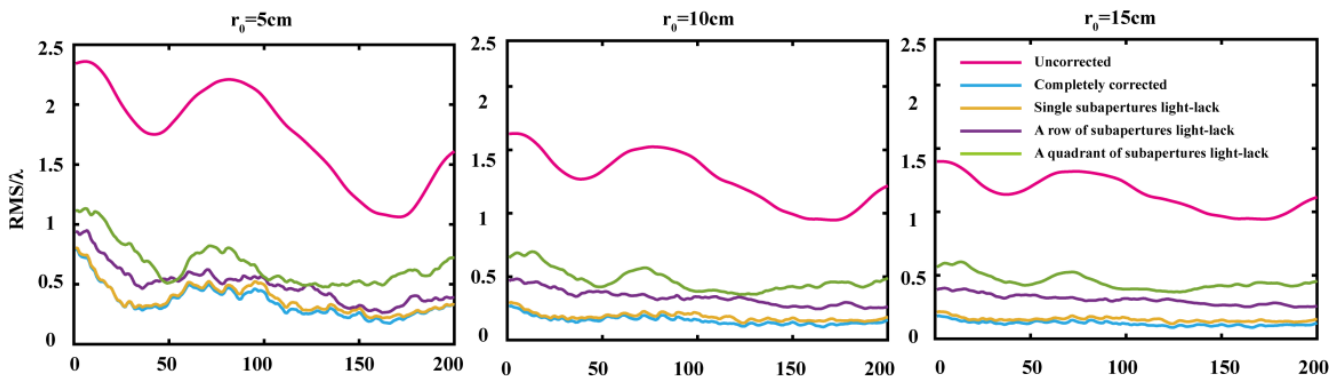


Figure 12. Correction results of 200 frames under different situations of under-sampling, for r_0 are 5 cm, 10 cm, and 15 cm, respectively. The pinkish red line represents the uncorrected aberrant wavefront distorted by the turbulence, the blue line represents the turbulence was corrected with all the sub-apertures were illuminate, the yellow line represents a single sub-aperture lack of light, the purple line represents a row of sub-apertures lack of light, the green line represents a quadrant of sub-apertures lack of light.

The RMS of the corrected wavefront for the mixed aberrations under different atmospheric conditions was analyzed, as shown in Figure 13. Firstly, the RMS is decreased when r_0 is increased, and the RMS tends to converge when r_0 exceeds 9 cm, indicating that for a certain AO system, the impact of the atmospheric turbulence becomes faded. In addition,

compared with the uncorrected wavefront, the RMS can be reduced by a factor of 3.5 and 5~8 for a row of sub-apertures under-sampling and a single sub-aperture under-sampling respectively. But for the aberrant wavefront under-sampled by a quadrant of sub-apertures, the RMS can be reduced by a factor of 3, which means the turbulence can be partially corrected effectively.

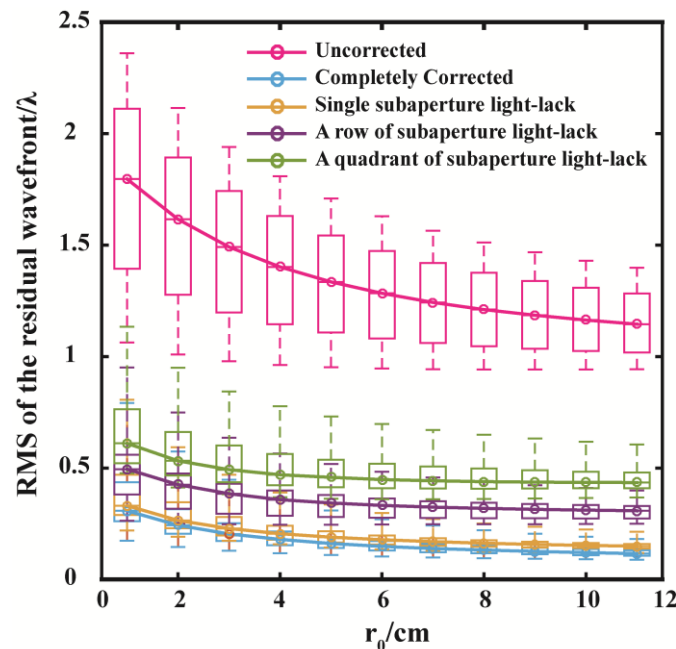


Figure 13. For the case of mixed aberration wavefront, RMS of the residual wavefront varies with different values of r_0 under the conditions of uncorrected, completely corrected, single sub-aperture lack of light, a row of sub-apertures lack of light, and a quadrant of sub-apertures lack of light. The RMS of the three cases with under-sampling can be reduced by a factor of 5~8, 3.5, and 3 compared with the uncorrected result.

As in our analysis, the focal spots in adjacent sub-apertures may be confused while the turbulence was so strong, and the dynamical range was not enough, thus some sub-apertures would lack light. The holographic Shack-Hartmann wavefront sensor based on the correlation peak displacement detection [33] may become a useful tool, which modulated the incident aberrant wavefront with an SLM instead of a microlens array, then discriminable patterns were reconstructed from the micro-hologram array on each detection area, which can be expanded to adjacent areas with a dynamical range up to $\pm 5\lambda$ [34]. Thus the sub-apertures lack of light caused by the dynamical range insufficient can be addressed, and it would be studied in our next step work.

5. Conclusions

The large ground-based telescope was equipped with an AO system to mitigate the turbulence disturbance, we analyzed the impact of the under-sampling of S-H WFS on the wavefront reconstruction, the speed of our wavefront reconstruction was 2000 Hz, and the sensitivity was $10\mu\text{rad}$. For three typical cases of under-sampling, i.e., a single sub-aperture lack of light induced by damage of the sub-microlens, a row sub-aperture lack of light induced by pupil shifting, and a quadrant sub-aperture lack of light induced by performance degradation of the detector. The differences between the reconstructed wavefront in these three cases and the reconstructed wavefront completed sampled were compared. Some conclusions were summarized as follows:

1. For a typical atmospheric condition (r_0 is 10 cm), the influence of the under-sampling induced by a single sub-aperture lack of light on the dynamical aberration is negligible, the reconstructed wavefront is equivalent to that all the sub-apertures were

used to sample. With the increasing numbers of the sub-aperture under-sampling, the wavefront reconstruction error was significantly increased. Compared with the uncorrected wavefront, the RMS can be reduced by a factor of 5~8, 4~6, and 2~3 for a single sub-aperture, a row sub-apertures, and a quadrant sub-apertures under-sampling, respectively, using our proposed method.

2. For the most common statistical aberration (defocus) in the telescope optical path, the reconstructed wavefront was influenced by the position of the sub-apertures lack of light. The edge of the reconstructed wavefront was corrugated symmetrically when the aberrant wavefront was under-sampled with a single sub-aperture lack of light. The difference between the initial wavefront and the reconstructed wavefront is directly proportional to the number of sub-apertures that lack light. The under-sampling of the aberrant wavefront in these three cases has a greater influence on statistical aberration than the dynamical turbulence.

3. For the mixed aberrations (turbulence dynamical aberration and defocus aberration), the RMS for the corrected wavefront in these three cases tend to converge when r_0 exceeds 9 cm. Compared with the aberrant wavefront, the RMS can be reduced by a factor of 6, 3.5, and 3 for a single sub-aperture, a row of sub-apertures, and a quadrant of sub-apertures under-sampling, respectively.

Author Contributions: Conceptualization, J.H. and G.W.; methodology, J.H. and S.W.; investigation, J.H. and L.Y.; funding acquisition, J.H.; formal analysis, L.Y.; writing—original draft preparation, J.H. and G.W.; writing—review and editing, J.H. and S.W. All authors have read and agreed to the published version of the manuscript.

Funding: This work was supported by the National Natural Science Foundation of China (Grant No. 62105047), The Natural Science Foundation of Chongqing, China (Grant No. cstc2020jcyj-msxmX0727), Project of Science and Technology research program of the Chongqing municipal Education Commission (Grant No. KJQN201900805), China Postdoctoral Science Foundation (Grant No. 2021M703593), Chongqing Key Laboratory of Manufacturing Equipment Mechanism Design and Control, China (Grant NO.KFJJ2019074).

Institutional Review Board Statement: The study did not require ethical approval.

Informed Consent Statement: The study did not involve humans.

Data Availability Statement: Data is unavailable due to privacy.

Acknowledgments: We are thankful for the advice, guidance, and support given by Kai Wei, Kai Jin, and Keran Deng from the Key Laboratory on Adaptive Optics, Chinese Academy of Sciences. Last but not least, we thank all the other members of our group for their help.

Conflicts of Interest: The authors declare no conflict of interest.

References

1. Wang, J.; Songsheng, Y.; Li, Y.; Du, P.; Zhang, Z. A parallax distance to 3C 273 through spectroastrometry and reverberation mapping. *Nat. Astron.* **2020**, *4*, 517–525. [[CrossRef](#)]
2. Max, C. Introduction to adaptive optics and its history. In Proceedings of the American Astronomical Society 197th Meeting. NSF Center for Adaptive Optics University of California at Santa Cruz and DOE Lawrence Livermore National Laboratory, San Diego, CA, USA, 7–11 January 2001.
3. Hardy, J.W. *Adaptive Optics for Astronomical Telescope*; Oxford University Press: New York, NY, USA, 1998.
4. Babcock, H.W. The possibility of compensating astronomical seeing. *Publ. Astron. Soc. Pac.* **1953**, *65*, 229–236. [[CrossRef](#)]
5. Angel, J.R.P. Ground-based imaging of extrasolar planets using adaptive optics. *Nature* **1994**, *368*, 203–207. [[CrossRef](#)]
6. Platt, B.C.; Shack, R. History and principles of Shack–Hartmann wavefront sensing. *J. Refract. Surg.* **2001**, *17*, S573–S577. [[CrossRef](#)]
7. Rigaut, F. Astronomical Adaptive Optics. *Publ. Astron. Soc. Pac.* **2015**, *127*, 1197–1203. [[CrossRef](#)]
8. Valente, D.; Rativa, D.; Vohnsen, B. Wavefront sensing using a liquid-filled photonic crystal fiber. *Opt. Express* **2015**, *23*, 13005–13014. [[CrossRef](#)]
9. Wizinowich, P.L.; Le Mignant, D.; Bouchez, A.H.; Campbell, R.D.; Chin, J.C.Y.; Contos, A.R.; van Dam, M.A.; Hartman, S.K.; Johansson, E.M.; Lafon, R.E.; et al. The W. M. Keck Observatory Laser Guide Star Adaptive Optics System: Overview. *Publ. Astron. Soc. Pac.* **2006**, *118*, 297–309. [[CrossRef](#)]

10. Rigaut, F.; Neichel, B. Multiconjugate Adaptive Optics for Astronomy. *Annu. Rev. Astron. Astrophys.* **2018**, *56*, 277–314. [[CrossRef](#)]
11. Rigaut, F.; Neichel, B.; Boccas, M.; d’Oreville, C.; Vidal, F.; van Dam, M.A.; Arriagada, G.; Fesquet, V.; Galvez, R.L.; Gausachs, G.; et al. Gemini multiconjugate adaptive optics system review—I. Design, trade-offs and integration. *Mon. Not. R. Astron. Soc.* **2014**, *437*, 2361–2375. [[CrossRef](#)]
12. Benoit, N.; Lu, J.R.; François, R.; Ammons, S.M.; Carrasco, E.R.; Lassalle, E. Astrometric performance of the Gemini multiconjugate adaptive optics system in crowded fields. *Mon. Not. R. Astron. Soc.* **2014**, *445*, 500–514.
13. Hippler, S. Adaptive Optics for Extremely Large Telescopes. *J. Astron. Instrum.* **2019**, *8*, 1950001. [[CrossRef](#)]
14. Huang, J.; Wei, K.; Jin, K.; Li, M.; Zhang, Y. Controlling the Laser Guide Star power density distribution at Sodium layer by combining Pre-correction and Beam-shaping. *Opt. Commun.* **2018**, *416*, 172–180. [[CrossRef](#)]
15. Herrmann, J. Cross coupling and aliasing in modal wave-front estimation. *J. Opt. Soc. Am.* **1981**, *71*, 989–992. [[CrossRef](#)]
16. Hernández-Gómez, G.; Malacara-Hernández, Z.; Malacara-Hernández, D. Hartmann tests to measure the spherical and cylindrical curvatures and the axis orientation of astigmatic lenses or optical surfaces. *Appl. Opt.* **2014**, *53*, 1191–1199. [[CrossRef](#)]
17. Zhang, A.; Rao, C.; Zhang, Y.; Jiang, W. Sampling error analysis of Shack–Hartmann wavefront sensor with variable subaperture pixels. *J. Mod. Opt.* **2004**, *51*, 2267–2278.
18. Baranec, C.; Dekany, R. Study of a MEMS-based Shack-Hartmann wavefront sensor with adjustable pupil sampling for astronomical adaptive optics. *Appl. Opt.* **2008**, *47*, 5155–5162. [[CrossRef](#)]
19. Bond, C.Z.; Correia, C.; Teixeira, J.; Sauvage, J.; Véran, J.; Fusco, T. Anti-aliasing wave-front reconstruction with Shack-Hartmann sensors. *Adapt. Opt. Extrem. Large Telesc. 4-Conf. Proc.* **2015**, *1*.
20. Correia, C.M.; Teixeira, J. Anti-aliasing Wiener filtering for wave-front reconstruction in the spatial-frequency domain for high-order astronomical adaptive-optics systems. *J. Opt. Soc. Am. A* **2014**, *31*, 2763–2774. [[CrossRef](#)]
21. Hernández, Z.M.; Doblado, D.M.; Hernández, D.M. Least-squares fitting of hartmann or shack-hartmann data with a circular array of sampling points. *Appl. Opt.* **2015**, *54*, E113–E122. [[CrossRef](#)]
22. Vieggers, M.; Brunner, E.; Soloviev, O.; de Visser, C.C.; Verhaegen, M. Nonlinear spline wavefront reconstruction through moment-based shack-hartmann sensor measurements. *Opt. Express* **2017**, *25*, 11514–11529. [[CrossRef](#)]
23. Patti, M.; Lombini, M.; Schreiber, L.; Bregoli, G.; Arcidiacono, C.; Cosentino, G.; Diolaiti, E.; Foppiani, I. Prototype of a laser guide star wavefront sensor for the Extremely Large Telescope. *Mon. Not. R. Astron. Soc.* **2018**, *477*, 539–547. [[CrossRef](#)]
24. Ping, W.; Xingyang, L.; Xi, L.; Jianfeng, L. Influence of lack of light in partial subapertures on wavefront reconstruction for shack-hartmann wavefront sensor. *Chin. J. Lasers* **2020**, *47*, 0409002. [[CrossRef](#)]
25. Liang, J.; Grimm, B.; Goelz, S.; Bille, J.F. Objective measurement of the wave aberrations of the human eye with the use of a Hartmann-Shack wave-front sensor. *J. Opt. Soc. Am. A* **1994**, *11*, 1949–1957. [[CrossRef](#)] [[PubMed](#)]
26. Wanek, J.; Mori, M.; Shahidi, M. The Effect of Aberrations and Scatter on Image Resolution Assessed by Adaptive Optics Retinal Section Imaging. *J. Opt. Soc. Am. A* **2007**, *24*, 1296–1304. [[CrossRef](#)] [[PubMed](#)]
27. Stockbridge, C.; Lu, Y.; Moore, J.; Hoffman, S.; Paxman, R.; Toussaint, K.; Bifano, T. Focusing through dynamic scattering media. *Opt. Express* **2012**, *20*, 15086–15092. [[CrossRef](#)]
28. Galaktionov, I.; Sheldakova, J.; Nikitin, A.; Samarkin, V.; Parfenov, V.; Kudryashov, A. Laser beam focusing through a moderately scattering medium using bimorph mirror. *Opt. Express* **2020**, *28*, 38061–38075. [[CrossRef](#)]
29. Changhui, R.; Wenhan, J.; Yudong, Z.; Ling, N.; Tang, G.; Li, M.; Shen, F.; Xu, B. 61-element adaptive optical system for 1.2 m telescope of Yunnan Observatory. *Chin. J. Quantum Electron.* **2006**, *23*, 295–302.
30. Ye, J.; Wang, W.; Gao, Z.; Liu, Z.; Wang, S.; Benítez, P.; Miñano, J.C.; Yuan, Q. Modal wavefront estimation from its slopes by numerical orthogonal transformation method over general shaped aperture. *Opt. Express* **2015**, *23*, 26208. [[CrossRef](#)]
31. Jiang, W.; Li, H. Hartmann-Shack wavefront sensing and wavefront control algorithm. *Proc. SPIE* **1990**, *1271*, 82–93.
32. Conan, R.; Correia, C. Object-oriented Matlab adaptive optics toolbox. *Proc. SPIE* **2014**, *9148*, 91486C.
33. Saita, Y.; Shinto, H.; Nomura, T. Holographic Shack–Hartmann wavefront sensor based on the correlation peak displacement detection method for wavefront sensing with large dynamic range. *Optica* **2015**, *2*, 411–415. [[CrossRef](#)]
34. Krasin, G.; Kovalev, M.; Stsepuro, N.; Ruchka, P.; Odinkov, S. Lensless Scheme for Measuring Laser Aberrations Based on Computer-Generated Holograms. *Sensors* **2020**, *20*, 4310. [[CrossRef](#)] [[PubMed](#)]

Disclaimer/Publisher’s Note: The statements, opinions and data contained in all publications are solely those of the individual author(s) and contributor(s) and not of MDPI and/or the editor(s). MDPI and/or the editor(s) disclaim responsibility for any injury to people or property resulting from any ideas, methods, instructions or products referred to in the content.